

Relativistic full-potential multiple scattering theory: An *ab initio* method and its applications

Xianglin Liu

Department of physics, Carnegie Mellon University

Yang Wang

Pittsburgh supercomputing center, Carnegie Mellon University

Markus Eisenbach

Center for computational sciences, Oak Ridge National Laboratory

G. Malcolm Stocks

Materials science and technology division, Oak Ridge National Laboratory

January 20, 2017

Abstract

The Green function plays an essential role in the Kohn-Korringa-Rostocker (KKR) multiple scattering method. In practice, it is constructed from the regular and irregular solutions of the local Kohn-Sham equation and robust methods exist for spherical potentials. However, when applied to potentials of general shape, combining the regular and irregular solutions can give rise to numerical problems at small radius. One common practice to avoid this problem is to stop using full potential within a small radius, but then the accuracy of the valence charge around origin is compromised. Here we present a full-potential implementation of relativistic full-potential KKR method to perform *ab initio* self-consistent calculation by directly solving the Dirac differential equation, which intrinsically incorporates the interesting relativistic effect of spin-orbit coupling. The numerical problem around the origin is eliminated by splitting the Green function into two parts and carrying out the energy integral along different contours. To facilitate the energy integral of the single-site Green function, a pole-searching technique is employed to identify the single-site

shallow bound states and resonance states. By singling out the localized valence electrons, this method provides a natural framework to incorporate correlation effects. To illustrate our method, test calculations are performed for polonium and noble metals, and a number of interesting relativistic effects are discussed.

1 Introduction

The multiple-scattering theory (MST) is a widely used electronic structure calculation method developed from the original KKR method introduced by Korringa [1], Kohn, and Rostoker [2]. This method not only demonstrates a natural separation between the potential and the structural properties, but also explicitly provides a way to calculate the Green function of the system, which can be used to extract physical variables such as total energy, charge density, and magnetic moments. The availability of Green function also makes MST a versatile tool and can be easily combined with other methods to investigate more complex systems. For example, by applying the Dyson's series expansion to the Green function, the disorders and impurities in an otherwise perfect crystal can be investigated. Another example is the combination of MST with coherent potential approximation (CPA) [3–5], which is widely applied to study random alloys. Finally, a more recent development is on studying the strongly correlated system, where the Green function from MST can be readily used in the GW approximation [6] and the dynamical mean field theory (DMFT) [7]. On the other hand, the real space formulation of MST [8] also demonstrates excellent linear scalability on current supercomputing architecture [9], and can be employed to study solid state systems with tens of thousands of atoms.

The MST originally solves the Schrödinger equation and employs the muffin-tin (MT) potential approximation, where the potential is spherically symmetric inside the muffin-tin sphere and is constant outside. The muffin-tin approximation generally works well for systems dominated by metallic bonding, but can not properly describe a wide range of systems where the asymmetries play an important role, such as surfaces, two-dimensional materials, and systems with directional covalent bonding. The Schrödinger equation is nonrelativistic and can not properly describe systems where relativistic effects are important. In particular, it doesn't account for the spin-orbit coupling (SOC), which attracts a lot of interest recently due to the important role it plays in many technically important phenomenon, such as magnetocrystalline anisotropy, Rashba effect, and magnetic Skyrmion [10]. The widely used scalar-relativistic approximation [11] also doesn't include SOC,

although correction can be made in a perturbative second-variational way. To take into account both the relativistic effects and the full-potential effect on an equal footing, the MST need to be extended to the full-potential scheme and be capable of solving the Dirac equation. Much work has been done by different groups on the fully relativistic full potential scheme [12–18], among them the most widely used implementation is developed by Huhne *et al* [15] to either solve the coupled integral equations or directly solve the coupled differential equations.

In MST the Green functions are constructed from the regular and irregular solutions of the Kohn-Sham equations. A persistent problem in standard implementation of full-potential MST is that the numerical errors of the irregular solutions are very difficult to control near the origin [19]. As a result, the charge density calculated from the Green function will be pathological within a sizable fraction of the muffin-tin radius. This pathology is originated from the coupling of solution components with different angular momentum indices l , and it gets worse as the angular momentum cutoff l_{max} increases. The practice employed by Huhne *et al* is to discard the non-spherical components of the potential within a cutoff radius r_{ns} , with the argument that close to the nucleus the non-spherical contributions to the potential are small. This practice becomes problematic for $l_{max} \geq 4$ because then r_{ns} will not be small. As a result, the non-spherical components of the potential can have a significant impact on the valence charge density around the origin, and affect the accuracy of the Hellmann-Feynman forces calculated. In Ref. [20] it is proposed to use a sub-interval technique to systematically decrease the numerical error by reducing the step size when approaching the origin. This method still requires spherical potential approximation within a small radius, and is also less effective for large l_{max} .

To completely get rid of this pathology, we use an approach that requires no evaluation of the irregular solutions. This is achieved by splitting the full Green function into two parts and carrying out the energy integral along different contours on the complex plane. The first part correspond to the single-site Green function, and the second part is the remaining multiple scattering Green function. The irregular solutions only show up in the single-site Green function. As we will show in section 2, if the energy integration of the single-site Green function is carried out along real axis, the irregular solutions will make no contribution to the charge density. Actually this method was presented in a previous paper [19] but was considered impractical because the sharp resonance states are laborious to integrate on real axis. However, by making use of an efficient pole-searching algorithm come up by one of the authors, Y. Wang, we find this real axis energy integral can be accomplished much faster with a weighted sampling technique. Other

than the numerical benefits, this pole-searching technique identifies both the shallow bound states and the resonance states. By projecting out these localized electron orbitals, correlation correction schemes such as LDA+U [21] and self-interaction correction (SIC) [22, 23] can then be incorporated into our method.

In the following section we will first explain the energy integration scheme, then we will show how the poles of the single-site Green function can be used to facilitate the energy integration of the shallow bound states and the resonance states. Details of this pole-searching technique are presented in section 3. In section 4 polonium is used as an example to demonstrate our method. In section 5 the density of states and bulk properties of copper, silver, and gold are calculated as applications of our method. Two examples of relativistic effects, origin of the color of gold and the simple cubic structure of polonium are also discussed in the last two sections.

2 Methods

The two physical quantities of interest to us the most in the present context are the the integrated density of states $N(E)$ and the charge density $\rho(\mathbf{r})$. In a typical *ab initio* calculation, both two quantities need to be evaluated at each self-consistent loop to determine the new Fermi energy and effective potential. In MST, the charge density is obtained from the energy integral of the Green function,

$$\rho(\mathbf{r}) = -\frac{1}{\pi} \text{Im} \text{Tr} \int_{E_b}^{E_F} G(E, \mathbf{r}, \mathbf{r}) dE, \quad (1)$$

where E_b is the lowest energy in the conduction band, E_F is the Fermi Energy. The integrated density of states (IDOS) is given by the energy integral of the density of states (DOS) $n(E)$

$$N(E) = \int_{E_b}^E n(E') dE', \quad (2)$$

and $n(E)$ is calculated from the volume integral of the Green function

$$n(E) = -\frac{1}{\pi} \text{Im} \text{Tr} \int_{\Omega} G(E, \mathbf{r}, \mathbf{r}) d\mathbf{r}. \quad (3)$$

The Green function is obtained by solving the Dirac-Kohn-Sham equation and the details has been given in Ref. [18]. Note that the energy integration is needed in the calculation of both $N(E)$ and $\rho(\mathbf{r})$, but a simple real energy

integration scheme is unfeasible for bulk materials because the corresponding multiple scattering Green functions have large numbers of poles on the real energy axis. One resolution of this problem is to carry out the integral along a contour in the complex energy plane, with the observation that the Green function is holomorphic except for poles at the bound states and a cut on the real axis starting at E_b . In principle, this method would be very efficient. The Green function is smooth as a function of the complex energy, therefore if the Gaussian quadrature integration method are used, only a few dozen energy points are needed to reach a high accuracy. In practice, however, the implementation is hindered by the presence of the irregular solutions in the expression of the Green function, which is commonly written as [18]

$$G(E, \mathbf{r}, \mathbf{r}') = \sum_{\Lambda\Lambda'} Z_{\Lambda}(E, \mathbf{r}) \tau_{\Lambda\Lambda'}(E) Z_{\Lambda'}^+(E, \mathbf{r}') - \sum_{\Lambda} Z_{\Lambda}(E, \mathbf{r}) \mathcal{J}_{\Lambda}^+(E, \mathbf{r}'). \quad (4)$$

where $Z_{\Lambda}(E, \mathbf{r})$ and $Z_{\Lambda}^+(E, \mathbf{r})$ are the right-hand and left-hand regular solutions, respectively, $\mathcal{J}_{\Lambda}^+(E, \mathbf{r}')$ are the left-hand irregular solutions, and $\tau_{\Lambda\Lambda'}(E)$ are the scattering-path matrices. The irregular solutions are singular at the origin and are obtained by integrating inward from outside. Unfortunately they typically have unacceptable numerical errors near the origin, which introduce the aforementioned pathology to the charge density for the following reason: In full-potential scheme, the non-spherical potential components couple the solutions with different l index. Near the origin, the irregular solutions diverges as r^{-l-1} , and the coupling to channels of higher l would amplify the numerical round-off error in the irregular solutions and ruin the whole differential equation solver.

In our approach, the elimination of this pathological behavior of the Green function is accomplished by spitting the Green function into the single-site scattering part G_s and the remaining multiple scattering part G_m

$$G(E, \mathbf{r}, \mathbf{r}') = G_s(E, \mathbf{r}, \mathbf{r}') + G_m(E, \mathbf{r}, \mathbf{r}'). \quad (5)$$

The explicit expression of the $G_s(E, \mathbf{r}, \mathbf{r}')$ is

$$G_s(E, \mathbf{r}, \mathbf{r}') = \sum_{\Lambda\Lambda'} Z_{\Lambda}(E, \mathbf{r}) t_{\Lambda\Lambda'}(E) Z_{\Lambda'}^+(E, \mathbf{r}') - \sum_{\Lambda} Z_{\Lambda}(E, \mathbf{r}) \mathcal{J}_{\Lambda}^+(E, \mathbf{r}'), \quad (6)$$

where $t_{\Lambda\Lambda'}(E)$ is the single-site t matrix. For simplicity of the discussion, we only consider one atom per unit cell, noticing that generalization to complex lattices are straightforward. The explicit expression of $G_m(E, \mathbf{r}, \mathbf{r}')$ is

$$G_m(E, \mathbf{r}, \mathbf{r}') = \sum_{\Lambda\Lambda'} Z_{\Lambda}(E, \mathbf{r}) (\tau_{\Lambda\Lambda'}(E) - t_{\Lambda\Lambda'}) Z_{\Lambda'}^+(E, \mathbf{r}'). \quad (7)$$

Note that the $Z\mathcal{J}$ term in $G_s(E, \mathbf{r}, \mathbf{r}')$ is real for real energies, so it will vanish when the imaginary part is taken. Therefore, by carrying out the integration over real energy axis, the irregular solutions no longer need to be evaluated. As for the multiple scattering part $G_m(E, \mathbf{r}, \mathbf{r}')$, noticing that it is holomorphic on the upper half-plane because both $G_s(E, \mathbf{r}, \mathbf{r}')$ and $G(E, \mathbf{r}, \mathbf{r}')$ are, we simply carry the integration along a semi-circle contour, as shown in figure 1.

To efficiently evaluate the energy integral of $G_s(E, \mathbf{r}, \mathbf{r}')$, two obstacles need to be overcome. The first one is the sharp resonance states, examples of which are the d resonances in noble metals [18] and the p resonances of polonium, as shown in figure 2. In relativistic full potential schemes, these resonance peaks usually become sharper and split into multiple peaks on DOS plots due to spin-orbit coupling and crystal field splitting, and make a straightforward energy integration even more prohibitive. Another obstacle is the shallow bound states of the valence electrons which render a direct integration on the real axis unfeasible. These shallow bound states show up, for example, in our calculation of polonium, and corresponds to poles of the Green function on the negative real axis, as shown in table 1.

The resonance peaks are originated from the poles located at the forth quadrant in the complex plane. As will be explained in the following, these peaks are well approximated by the Lorentzian functions, and the energy integration at the positive axis can be carried out efficiently with a weighted sampling technique. First, in analogy to the bound states in the spectral expression of the single-site Green function, around the resonance states, the single-site Green function can be approximated by

$$G_s(E, \mathbf{r}, \mathbf{r}')|_{E \approx E_n} \approx \frac{\psi_n(E, \mathbf{r})\psi_n^\dagger(E, \mathbf{r}')}{E - (E_n - i\lambda_n)}, \quad (8)$$

where the complex resonance energy has been written in terms of the real and imaginary part as $E_n - i\lambda_n$. Next we plug equation (8) into equation (3) and use the normalization condition of the wave function

$$\int_{\Omega} \psi_n(\mathbf{r})\psi_n^\dagger(\mathbf{r})d\mathbf{r} = 1, \quad (9)$$

then the density of states around E_n becomes

$$n(E)|_{E \approx E_n} \approx -\frac{1}{\pi} \text{Im} \left(\frac{1}{E - E_n + i\lambda_n} \right) = \frac{1}{\pi} \frac{\lambda_n}{(E - E_n)^2 + \lambda_n^2}, \quad (10)$$

which is exactly a Lorentzian function. The values of E_n and λ_n are determined using the pole-searching technique detailed in section 3. Now that the

approximate behaviors of the peaks are known, we can construct a weighted energy mesh to carry out the integration, i.e., the energy mesh is chosen to be denser around the resonance peaks. To use this method, we need to find an appropriate cumulative distribution function $F(E)$. Here it is chosen to be

$$F(E) = \sum_n \frac{1}{\pi} \arctan \left(\frac{E - E_n}{\lambda_n} + \frac{1}{2} \right) + \frac{V}{3\pi^2} E^{3/2}, \quad (11)$$

where the first part is the integral of the Lorentzian function and the second part is to account for the non-resonance states, with V to be the volume of the unit cell. The weighted energy mesh is obtained by uniformly choosing points F_i between $F(0)$ and $F(E_F)$, then solving the inverse of $F(E)$ with, for example, bisection method.

For shallow bound states, the above weight sampling technique no longer works because now the Lorentzian function evolves into a Dirac delta function. We instead carry out the energy integration on small contours encircle the poles, as shown in figure (1). The reason that radius of the contour need to be small is to reduce the error caused by not carrying out the integration strictly on real axis. Although calculating the residue analytically is possible, in practice we still use the small contour method because it is simple to implement and yields accurate results, with the radius of contour chosen to be 10^{-4} Ry. Finally, as mentioned in the introduction, the regular solutions calculated at the poles can be used as local orbitals for treatment of electron correlations in the future.

The numerical parameters used in the calculation is as follows: The angular momentum cut-off of the wave function is chosen to be $l_{max} = 4$ and 4096 k-points is used. The number of energy points used in the weighted sampling integration is 100. The number of Gaussian energy points to integrate $G_m(E, \mathbf{r}, \mathbf{r}')$ is 30 for the large semi-contours, and 5–10 for the small contours around shallow bound states.

3 Pole searching technique

In scattering theory, the bound states and resonance states correspond to the poles of the S-matrix $\mathbf{S}(E)$ on complex energy plane, which in our formalism [18] is written as

$$\mathbf{S}_{\Lambda\Lambda'}(E) = [-iS_{\Lambda\Lambda'}(E) - C_{\Lambda\Lambda'}(E)] [iS_{\Lambda\Lambda'}(E) - C_{\Lambda\Lambda'}(E)]^{-1}, \quad (12)$$

where $S_{\Lambda\Lambda'}(E)$ and $C_{\Lambda\Lambda'}(E)$ are the sine and cosine matrices and Λ stands for the spin-angular indices κ, μ . To find the poles of S-matrix we only need

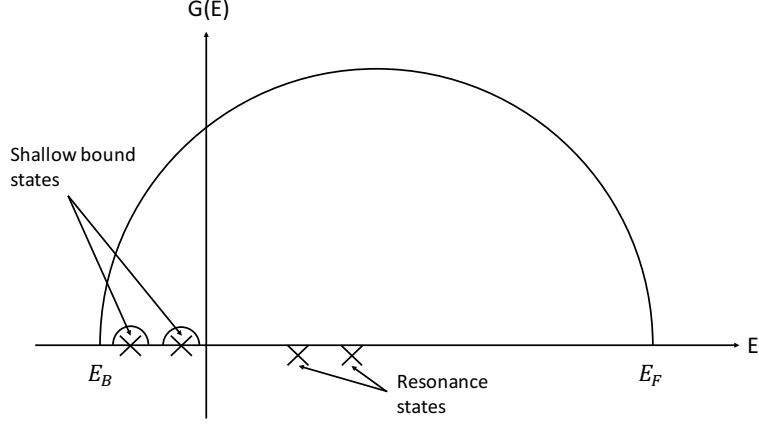


Figure 1: To avoid using the irregular solutions, the energy integral of the Green function is splitted into two parts. The multiple scattering part G_{mst} is integrated along the semi-circle contour, while the single-site part G_{ss} is integrated on real axis. The shallow bound states are integrated with a tiny circle and the resonance states are integrated using weighted sampling technique .

to identify the zeros of the Jost matrix $J_{\Lambda\Lambda'}(E)$, which is given by

$$J_{\Lambda\Lambda'}(E) = iS_{\Lambda\Lambda'}(E) - C_{\Lambda\Lambda'}(E). \quad (13)$$

In fact, the Jost matrix is a more fundamental quantity than the S matrix because it has no redundant zeros [24]. To efficiently determine the zeros of Jost matrix, a linear algebra method is used. Let us consider a square matrix $\underline{J}(z)$ of size $L \times L$, and we need to find its zeros, z_p , such that

$$\det [\underline{J}(z_p)] = 0. \quad (14)$$

Assuming that we are only interested in finding the poles, ϵ_p , which could correspond to the resonance states ($\epsilon_p > 0$) in the valence band or the shallow bound states ($\epsilon_p < 0$). We choose an energy, ϵ_0 , somewhere near a pole, and we call ϵ_0 the pivotal energy for our quadratic expansion of the matrix around ϵ_0 as follows,

$$\underline{J}(z) = \underline{J}(\epsilon_0 + \lambda) = \underline{J}^{(0)}(\epsilon_0) + \underline{J}^{(1)}(\epsilon_0)\lambda + \underline{J}^{(2)}(\epsilon_0)\lambda^2 \quad (15)$$

with $\lambda = z - \epsilon_0$. To find the zeros of this quadratic equation, we consider an alternative matrix,

$$\underline{A}(\lambda) = [\underline{J}^{(2)}(\epsilon_0)]^{-1} \underline{J}(\epsilon_0 + \lambda). \quad (16)$$

By multiplying $\left[\underline{J}^{(2)}(\epsilon_0)\right]^{-1}$ on both sides of equation (15), we get the following expansion,

$$\underline{A}(\lambda) = \lambda^2 - \underline{B}\lambda + \underline{C}, \quad (17)$$

where

$$\underline{B} = -\left[\underline{J}^{(2)}(\epsilon_0)\right]^{-1} \underline{J}^{(1)}(\epsilon); \quad \underline{C} = \left[\underline{J}^{(2)}(\epsilon_0)\right]^{-1} \underline{J}^{(0)}(\epsilon), \quad (18)$$

Obviously, $\underline{A}(\lambda)$ has the same zeros as $\underline{J}(\epsilon_0 + \lambda)$ at $\lambda_p = \epsilon_p - \epsilon_0$. We rewrite equation (17) as follows

$$\underline{A}(\lambda) = \lambda^2 - \underline{B}(\lambda - \underline{D}), \quad (19)$$

where

$$\underline{D} = \underline{B}^{-1}\underline{C} = -\left[\underline{J}^{(1)}(\epsilon_0)\right]^{-1} \underline{J}^{(0)}(\epsilon). \quad (20)$$

The following determination equation

$$\det [\underline{A}(\lambda)] = \det [\lambda^2 - \underline{B}(\lambda - \underline{D})] = 0 \quad (21)$$

is equivalent to

$$\det \begin{bmatrix} \lambda - \underline{D} & -\underline{I} \\ \underline{D}^2 & \lambda - \underline{B} + \underline{D} \end{bmatrix} = 0. \quad (22)$$

The eigenvalues λ_p ($p = 1, 2, \dots, 2L$) that satisfy this secular equation can be quickly found by diagonalizing the following matrix:

$$\begin{bmatrix} \underline{D} & \underline{I} \\ -\underline{D}^2 & \underline{B} - \underline{D} \end{bmatrix} \quad (23)$$

The zeros of matrix $S(z)$ are thus at $z_p = \lambda_p + \epsilon_0$. In practice, a simple way for computing the quadratic expansion coefficient matrices in equation (15) is to calculate $\underline{J}(z)$ at three energy values: $\epsilon_0 - \lambda$, ϵ_0 , $\epsilon_0 + \lambda$, with λ a small value, then solve the quadratic expansion equations. To search the poles within E_b and E_F , a set of panels on real energy axis is set up and ϵ_0 is chosen at the center of each panel and iteration can be utilized to improve the accuracy.

4 Calculation of Polonium

To illustrate the method we used, a test calculation of polonium is shown in this section. The reasons to use polonium as an example are as follows. First, polonium is a dangerous element with strong radioactivity, which makes experimental investigation of its physical property very difficult. Therefore, the *ab initio* calculation of polonium provides an important tool to reveal the physical properties of Po that are difficult to access by experiment. Second, polonium demonstrates some interesting characteristics, among them the most unique one is its simple cubic structure, which distinct itself from all the other elements as the only one crystallizing in this structure at room temperature. It's generally agreed this simple cubic structure is caused by relativistic effects [25, 26], although there are still debates on whether the stability of the simple cubic structure is caused by spin-orbit (SO) coupling or the mass-velocity and Darwin terms [25–27]. Finally, polonium has both shallow bound states and resonance states in the single-site Green function, therefore it is an ideal example to test our method.

Table 1: The poles of the single-site Green function of Po

Pole Number	real part	imaginary part
1	-0.68202472D+00	0.16325374D-15
2	-0.68202472D+00	-0.21372993D-15
3	-0.35205135D-01	-0.12391130D-13
4	-0.35205135D-01	0.11887440D-13
5	0.66052385D-01	-0.37929455D-01
6	0.66052385D-01	-0.37929455D-01
7	0.66052385D-01	-0.37929455D-01
8	0.66052385D-01	-0.37929455D-01

The poles of polonium obtained with our pole-searching algorithm are listed on table 1. The first two *s* poles and the following two *p* poles have negative real part and negligible imaginary part, which are the characteristics of shallow bound states. The other four *p* poles are on the forth quadrant of the complex plane and correspond to the resonance states. The single-site DOS and the total DOS of the system are shown in figure 2 and a comparison with the scalar relativistic + SO interaction calculation results in Ref. [27] yields excellent agreement. As pointed out in Ref. [27], the large separation between the 6*s* and 6*p* states in figure 2 is due to the inert pair effect. We can also see the splitting of the d electrons caused by SO interaction, from both the poles in table 1 and the DOS plots in figure 2. The total energy

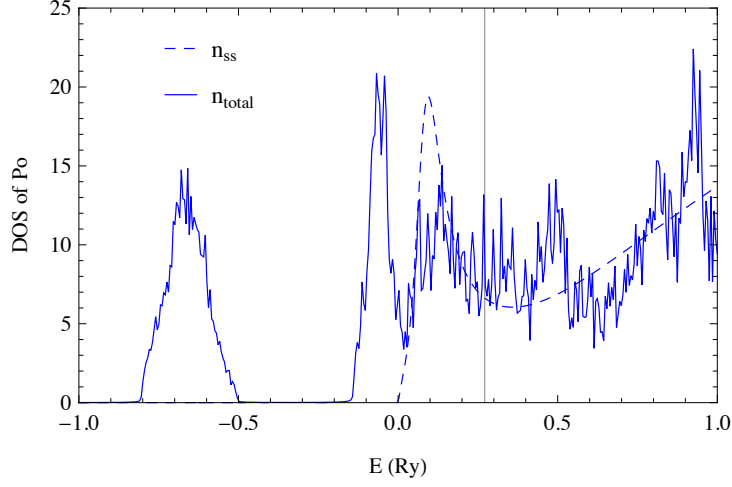


Figure 2: (Color online) Comparison of the total DOS and the single-site DOS of polonium. The dashed line is the single-site DOS and the solid line is the total DOS. The vertical line is the Fermi energy. The shallow bound states are not shown on the single-site DOS because they are essentially a set of Dirac δ functions.

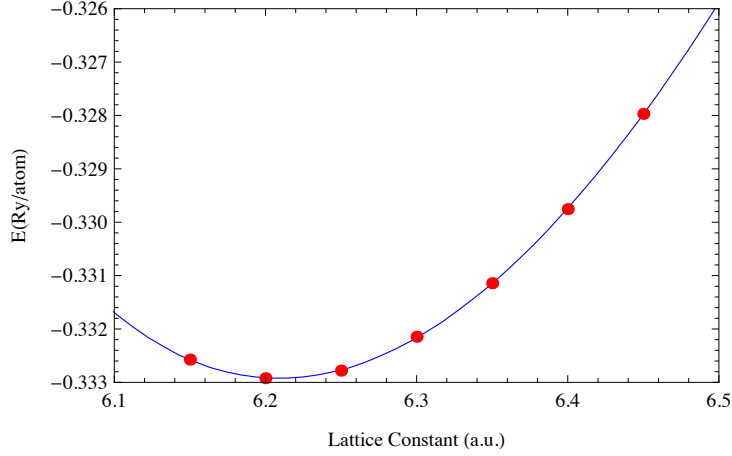


Figure 3: (Color online) The total energy vs lattice constant plot of polonium. A constant is subtracted from the total energy. The red dots are the calculated total energies using different lattice constants. The blue solid line is the fitted equation of state.

vs lattice constant plot is shown in figure 3, from which we find the lattice constant is 3.285 \AA , which is in good agreement with the experimental value of 3.345 \AA [28]. The bulk modulus is found to be 51.1 GPa , which also agrees

with the other first principle calculation results [26, 29].

5 Calculation of Cu, Ag, and Au

Table 2: Comparison of calculated lattice constants and bulk moduli of noble metals with the experimental values. LDA is employed in all calculations. Fully relativistic schemes are used except for the last two columns. In column Au_{NR} all electrons are calculated with nonrelativistic schemes, and relativistic schemes are utilized only for valence electrons in column Au_{R-Core}.

	Cu	Ag	Au	Au _{NR}	Au _{R-Core}
Lattice constants (a.u.)	6.65	7.55	7.60	8.05	8.20
Experiment	6.84	7.72	7.71		
Bulk Modulus (Mbar)	1.91	1.41	2.08	1.20	0.93
Experiment	1.37	1.01	1.80		

In this section we present the calculation results of copper, silver, and gold. Comparison of the calculated bulk properties with the experimental values are shown in table 2 and the total energy vs lattice constant plot of Au is shown in figure 5 as an example. Evidently, the relativistic MST calculation underestimate the lattice constants and overestimate the bulk modulus, which is a well-know characteristic of LDA. As demonstrated in Ref. [30], by employing GGA instead of the LDA functional, much better agreement with the experimental data can be obtained. In the last two columns of table 2, the nonrelativistic and partial relativistic results of Au are also shown to demonstrate the importance of relativity. The density of states of each element is shown in figure 4 and they are in good agreement with the results in Ref. [31]. A comparison with the nonrelativistic results is also made to investigate the relativistic effects. As we can see from the plots, in all nonrelativistic calculations, the DOS have five peaks, which is a result of the crystal field symmetry. under the impact of the spin-orbit coupling, these peaks further split to small peaks. The differences between relativistic and nonrelativistic results grow as the atomic numbers increase. For silver and gold, the *d* bands from relativistic calculation expand and moves closer to the Fermi energy. This is a result of relativistic contraction of the inner shell *s* electrons, whose relativistic effects are more significant than the *d* electrons. Actually this is the well-known explanation to the color of gold: due to relativistic effects, the transition energy between 5*d* and 6*s* decreases,

which absorbs the blue lights and reflects the lights seen as the golden to us. The relativistic effects in silver is small compared to gold, therefore it still reflects all the visible lights. Concerning the energy difference between top of the d band and the Fermi energy in the relativistic plots, we find they are small compared to the photoemission experimental results [32, 33]. But this is just a typical feature of DFT calculations, and is shown to be largely corrected [34] by using GW method to account for the self-energy effects.

6 Conclusions

We implemented a new approach to full-potential relativistic MST. By splitting the Green function into two parts and carrying out the energy integration along different contours, this method requires no evaluation of the irregular solutions and therefore is free of the pathology of the charge density near the origin. By explicitly searching the poles of the single-site Green function, we devised an efficient integration scheme to solve the numerical problems caused by the shallow bound states and the resonance states. The density of states and bulk modulus of polonium are calculated, with the lattice constant found to be 3.285 Å and the bulk modulus $B = 51.1$ GPa. As a test of our code, we also calculated the DOS and bulk modulus of Cu, Ag, and Au and compared them with experimental results.

7 Acknowledgements

This work has been sponsored by the U.S. Department of Energy, Office of Science, Basic Energy Sciences, Material Sciences and Engineering Division (M.E. and the later work of G.M.S) and by the Center for Defect Physics, an Energy Frontier Research Center of the Office of Basic Energy Sciences of the U. S. Department of Energy.

References

- [1] J. Korringa. *Physica*, 13:392, 1947.
- [2] W. Kohn and N. Rostoker. *Phys. Rev.*, 94:1111, 1953.
- [3] P. Soven. *Phys. Rev.*, 156:809, 1967.
- [4] B. L. Gyorffy. *Phys. Rev. B*, 1:3290, 1970.

- [5] G. M. Stocks, R. W. Williams, and J. S. Faulkner. *Phys. Rev. B*, 4:4390, 1971.
- [6] A. Ernst and M. Lüders. *Methods for band structure calculations in solids*. Springer: Berlin, 2004.
- [7] J. Minár, L. Chioncel, A. Perlov, H. Ebert, M. I. Katsnelson, and A. I. Lichtenstein. *Phys. Rev. B*, 72:045125, 2005.
- [8] Y. Wang, G. M. Stocks, A. W. Shelton, D. M. C. Nicholson, Z. Szotek, and W. M. Temmerman. *Phys. Rev. Lett.*, 75:2867, 1995.
- [9] M. Eisenbach, J. Larkin, J. Lutjens, S. Rennich, and J. H. Rogers. *Comput. Phys. Comm.*, 211:2, 2017.
- [10] S. Mühlbauer, B. Binz, F. Jonietz, C. Pfleiderer, A. Rosch, A. Neubauer, R. Georgii, and P. Böni. *Science*, 323:915–919, 2009.
- [11] D. D. Koelling and B. N. Harmon. *J. Phys. C: Solid State Phys.*, 10.16:3107, 1977.
- [12] E. Tamura. *Phys. Rev. B*, 45:3271, 1992.
- [13] S. C. Lovatt, B. L. Gyorffy, and G.-Y. Guo. *J. Phys.:Condens. Matter*, 5:8005, 1993.
- [14] X. Wang, X.-G. Zhang, W. H. Butler, G. M. Stocks, and B. N. Harmon. *Phys. Rev. B*, 46:9352, 1993.
- [15] T. Huhne, C. Zecha, H. Ebert, P. H. Dederichs, and R. Zeller. *Phys. Rev. B*, 58:10236, 1998.
- [16] M. Geilhufe, S. Achilles, M. A. Köbis, M. Arnold, I. Mertig, W. Hergert, and A. Ernst. *J. Phys.:Condens. Matter*, 27:435202, 2015.
- [17] H. Ebert, J. Braun, D. Ködderitzsch, and S. Mankovsky. *Phys. Rev. B*, 93:075145, 2016.
- [18] X. Liu, Y. Wang, M. Eisenbach, and G. M. Stocks. *J. Phys.: Condens. Matter*, 28:355501, 2016.
- [19] A. Rusanu, G.M. Stocks, Y. Wang, and J. S. Faulkner. *Phys. Rev. B*, 84:035102, 2011.
- [20] R. Zeller. *Phys. Status Solidi b*, 251:2048–54, 2014.

- [21] V. I. Anisimov, J. Zaanen, and O.K. Andersen. *Phys. Rev. B*, 44:943, 1991.
- [22] J. P. Perdew and A. Zunger. *Phys. Rev. B*, 23:1981, 1981.
- [23] M. Lüders *et al.* *Phys. Rev. B*, 71:205109, 2005.
- [24] S. A. Rakityansky, S. A. Sofianos, and K. Amos. *Nuov. Cim. B*, 111:363, 1996.
- [25] B. I. Min, J. H. Shim, M. S. Park, K. Kim, S. K. Kwon, and S. J. Youn. *Phys. Rev. B*, 73:132102, 2006.
- [26] D. Legut, M. Friák, and M. Šob. *Phys. Rev. Lett.*, 99:016402, 2007.
- [27] D. Legut, M. Friák, and M. Šob. *Phys. Rev. B*, 81:214118, 2010.
- [28] W. H. Beamer and C. R. Maxwell. *J. Chem. Phys.*, 14:569, 1946.
- [29] R. E. Kraig, D. Roundy, and M. L. Cohen. *Solid State Commun.*, 129:411, 2004.
- [30] N. Papanikolaou, R. Zeller, and P. H. Dederichs. *J. Phys.:Condens. Matter*, 14:2799, 1991.
- [31] A. H. MacDonald, J. M. Daams, S. H. Vosko, and D. D. Koelling. *Phys. Rev. B*, 25:713, 1982.
- [32] G. Panaccione *et al.* *J. Phys.: Condens. Matter*, 17:2671, 2005.
- [33] V. N. Strocov *et al.* *Phys. Rev. Lett.*, 81:4943, 1998.
- [34] A. Marini, G. Onida, and R. D. Sole. *Phys. Rev. Lett.*, 88:016403, 2002.

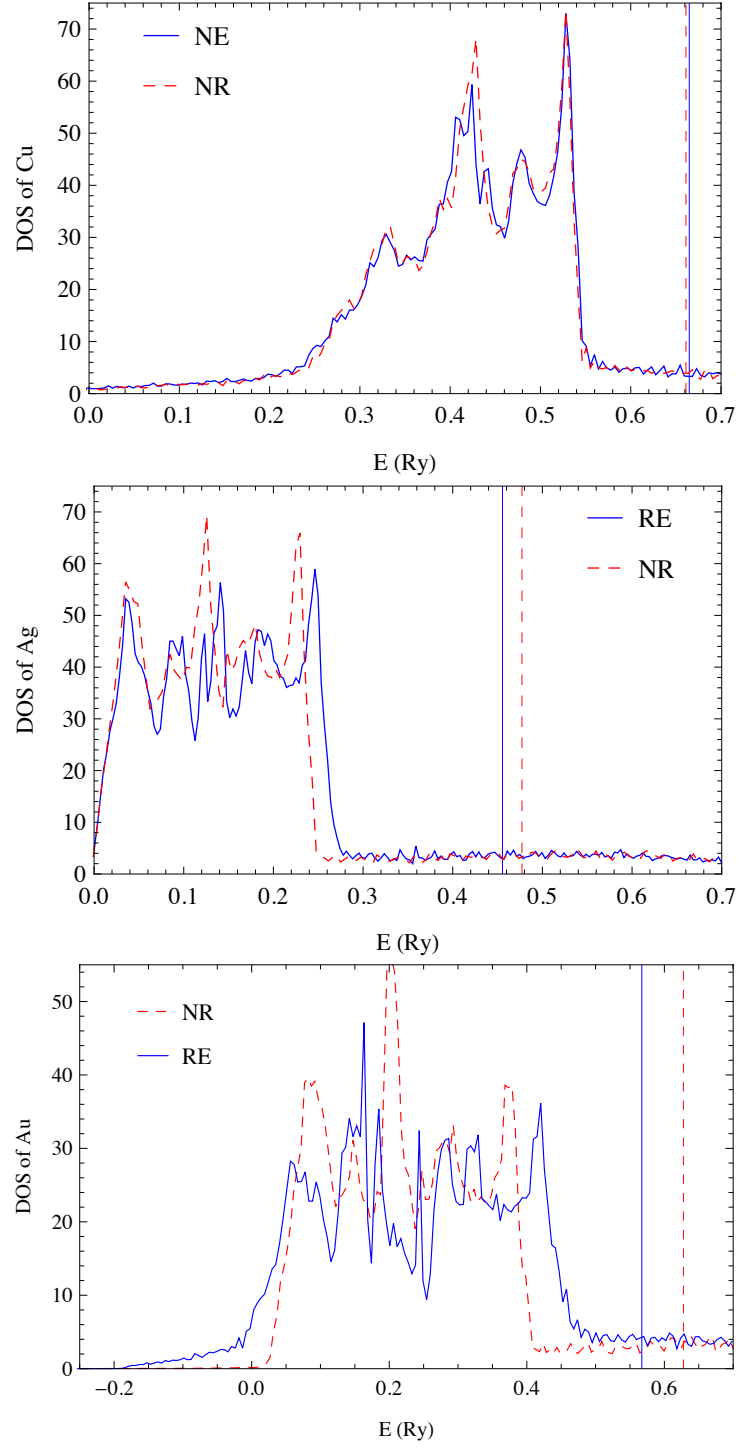


Figure 4: (Color online) Comparison of the relativistic and nonrelativistic DOS of Cu, Ag, and Au. The vertical lines are the Fermi energies. The red dashed lines are the nonrelativistic results and blue solid lines are the relativistic results.

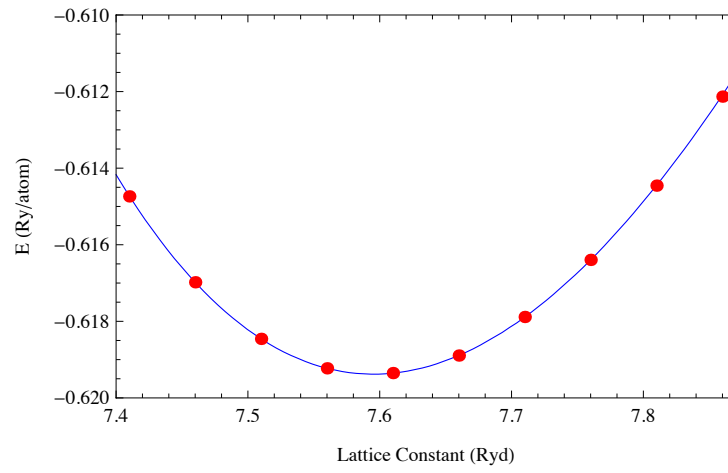


Figure 5: (Color online) The total energy vs lattice constant plot of Gold. A constant is subtracted from the total energy. The red dots are the calculated total energies using different lattice constants. The blue solid line is the fitted equation of state.